Environmental Science & Technology

pubs.acs.org/est

Article

Monolithic Catalyst of Ni Foam-Supported MnO_x for Boosting Magnetocaloric Oxidation of Toluene

Chunqi Wang, Shuangyong Su, Qiang Li, Xuelong Lv, Zhen Xu, Jin Chen,* and Hongpeng Jia*

Cite This: https://doi.org/10.1021/acs.est.3c09541

Read Online

ACCESS | Metrics & More | Article Recommendations | Supporting Information

ABSTRACT: Catalytic oxidation has been considered an effective technique for volatile organic compound degradation. Development of metal foam-based monolithic catalysts coupling electromagnetic induction heating (EMIH) with efficiency and low energy is critical yet challenging in industrial applications. Herein, a $Mn_{18.2}$-NF monolithic catalyst prepared by electrodeposition exhibited superior toluene catalytic activity under EMIH conditions, and the temperature of 90% toluene conversion decreased by 89 °C compared to that in resistance furnace heating. Relevant characterizations proved that the skin effect induced by EMIH encouraged activation of gaseous oxygen, leading to superior low-temperature redox properties of $Mn_{18.2}$-NF under the EMIH condition. *In situ* Fourier transform infrared spectroscopy results showed that skin effect-induced activation of oxidizing species further accelerated the conversion of intermediates. As a result, the $Mn_{18.2}$-NF monolithic catalyst under EMIH demonstrated remarkable performance for the toluene oxidation, surpassing the conventional nonprecious metal catalyst and other reported monolithic catalysts.

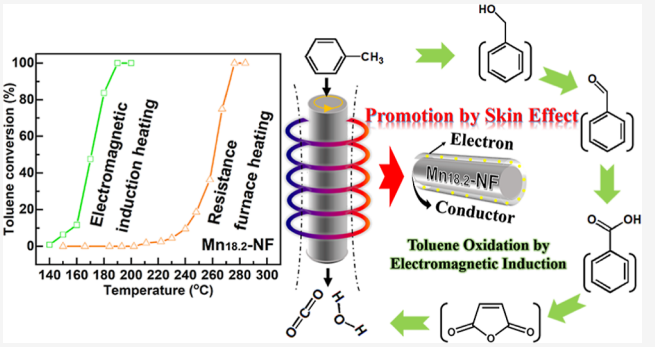

KEYWORDS: *catalytic oxidation, air pollution control, electromagnetic induction heating, volatile organic compounds, monolithic catalyst*

1. INTRODUCTION

Considering the widespread and increased usage of toluene, its evaporation gives rise to one typical pollutant of volatile organic compounds (VOCs), causing more risks to the environment and human beings.[1] Hence, more regulations are employed to restrict its massive emission, which has led to the thriving development of controlling technologies including thermal combustion, biologic degradation, photo/photothermal catalysis, thermocatalytic oxidation, and electrocatalytic oxidation.[2−5] Among the above techniques, thermocatalytic oxidation is the most promising method widely emerging for purification of the industrial exhaust, ascribed to its less secondary pollution and high efficiency.[6] Due to the advantages of low cost, substantial reserves, variable valence, and diverse crystal structures, non-noble metal-based catalysts have attracted wide attention.[7,8] Among them, manganese oxide (MnO_x) can be regarded as one of the most attractive candidates for toluene elimination. However, its relatively inferior catalytic activity compared with that of the noble metal-based catalysts would increase the energy consumption in the pollutant treatment process.

In recent years, to improve degradation efficiency and reduce energy consumption of pollutant treatment, intensive strategies by using the ion promotion effect, facet engineering, morphology control, element doping modification, and defect engineering have been developed.[1,5,9] From the perspective of reaction systems, there are also many studies that optimize catalytic combustion devices by equipping with exhaust heat exchangers, electric heating rods, airflow diaphragms, and processor covers to minimize heat loss.[10−13] In general, regenerative catalytic oxidation relying on ceramics honeycomb-based catalysts has recently been widely applied in industrial VOCs purification, resulting in a lower pressure drop and high thermal storage density.[14,15] However, its energy supply mode for catalytic combustion process always depends on electric power or fossil combustion heating, which leads to the problems of slow startup and low heat transfer efficiency. To counter this challenge, we had proposed to use ferromagnetic foam-based materials loaded with an active component and further coupled with electromagnetic induction heating (EMIH) to complete an enclosed circle of storage oxidation, which is fit to control the intermit source.[16−18] With the advantages of efficient heat transfer and rapid heating, EMIH has been demonstrated to economize on 98.9% of energy consumption compared with traditional

Received: November 14, 2023
Revised: December 15, 2023
Accepted: December 20, 2023

resistance furnace heating (RFH).[16] In addition to energy saving and flexible operation, the demanded temperature of catalysts could be reduced by EMIH compared to that in RFH according to the literature.[19,20] However, research studies aimed at understanding the promotion effect of EMIH are still rare. In our previous reports, the powders of Mn-based oxides and zeolite-supported Pt were loaded on Ni foam as an electromagnetic receptor.[16−18] The monolithic catalysts obtained by mechanical coating lacked structural connection between the catalytic site and magnetocaloric support, thereby resulting in no obvious difference of activity. Notably, Ni foam was chosen as the magnetocaloric support, which was reportedly used to prepare monolithic catalysts owing to its three-dimensional porous structure, good thermal conductivity, and unique mechanical plasticity. Recently, many studies have reported that monolithic catalysts of metal oxides grown on Ni foam exhibit good catalytic performance in the oxidation of VOCs.[21,22]

In order to enhance interaction between Ni foam and its supported composition, electrodeposition was applied to *in situ* graft manganese oxide (MnO_x) sheets on Ni foam to form a monolithic catalyst. Through modification of the deposition time, the amount of MnO_x loading was changed. The activities to catalyze toluene oxidation under EMIH varied with MnO_x loading as an inverted volcano curve. Among them, $Mn_{18.2}$-NF was chosen as the best option for EMIH-driven oxidation. Compared to that under RFH, the demanded temperature for 90% conversion of toluene on $Mn_{18.2}$-NF was reduced by 89 °C under EMIH, which was related to the skin effect induced by EMIH. By aligning EMIH with structural characterizations, it was observed that the EMIH-induced electron enrichment on the surface of Ni foam brought a negative electric field to the loaded MnO_x, which was favorable for the activation of the oxidizing species, causing better performance in eliminating toluene at low temperature.

2. MATERIALS AND METHODS

2.1. Chemicals and Materials. $(CH_3COO)_2Mn$, CH_3COONH_4, $(CH_3)_2SO$, and toluene were purchased from Sinopharm Chemical Reagent Co., Ltd. (Shanghai, China). All chemicals were of analytical grade and used as received without further purification.

2.2. Preparation of Catalysts. Monolithic catalysts of Ni foam-supported manganese oxides were synthesized by electrodeposition.[23] The Ni foam was ultrasonically cleaned with ethanol, acetone, and deionized water. Electrodeposition was carried out by a CHI 660D model electrochemical workstation with a two-electrode system, a piece of clean Ni foam (3.0 cm × 4.0 cm) as the working electrode and a carbon rod (φ = 8 mm) as the counter electrode. The manganese oxide nanosheets were electrodeposited in an aqueous solution of 0.01 M $(CH_3COO)_2Mn$, 0.02 M CH_3COONH_4, and 10 wt % $(CH_3)_2SO$ with a constant voltage of 1 V at 70 °C. The monolithic catalysts were named as Mn_x-NF (x = 1.6, 7.7, 18.2, and 25.3), where x refers to the actual Mn loads, which were determined by an X-ray fluorescence (XRF) spectrometer, as shown in Figure S1. In the control experiment, $Mn_{18.2}$-NF was treated by mechanical friction to enlarge the interval between the MnO_x layer and Ni surface, which was denoted as $Mn_{18.2}$-NF-S. To investigate the influence of EMIH treatment, $Mn_{18.2}$-NF was heated by EMIH in the air stream and the temperature was kept at 200 °C for different times, so the obtained sample was named $Mn_{18.2}$-NF-EMIH-X min (note: X = 5, 10, and 15 min). The pure NF sample was also treated *via* the same route only without the involvement of $(CH_3COO)_2Mn$, in which the Coulomb quantity is 180 C, named as NF.

2.3. Characterization. The samples were characterized by XRF, X-ray diffraction (XRD), Raman spectroscopy, scanning electron microscopy (SEM), transmission electron microscopy (TEM), X-ray photoelectron spectroscopy (XPS), H_2 temperature-programed reduction (H_2-TPR), O_2 temperature-programed desorption (O_2-TPD), toluene temperature-programed oxidation (Toluene-TPO), toluene temperature-programed surface reaction (Toluene-TPSR), Fourier transform infrared (FTIR) spectroscopy, and diffuse reflectance infrared Fourier transform spectroscopy (DRIFTS). An electrochemical workstation (CHI 660D, Shanghai CH Instruments) was used to measure the electromagnetic properties of the samples. The detailed procedures for characterization are described in the Supporting Information.

Especially, the redox property of $Mn_{18.2}$-NF monolithic catalysts under EMIH was studied by applying an electromagnetic temperature control device (Figure S2). Prior to H_2-TPR, the rolled-up monolithic catalyst was pretreated at 200 °C with a pure Ar stream of 30 mL/min flowing rate for 60 min and was cooled down to room temperature. Then, the stream was changed to 5% H_2/Ar, and the temperature was elevated from 30 to 240 °C at a rate of 10 °C/min with programed EMIH. Notably, a thermal conductivity detector (TCD) was applied to monitor the H_2-TPR process.

In addition, the reactant intermediates under EMIH were investigated by *in situ* FTIR spectroscopy, which was carried out on a Thermo Fisher is50 instrument. The monolithic sample was heated to 200 °C in an air stream to remove H_2O vapor and then was cooled to 25 °C. At this temperature, the IR spectrum was recorded as the background. Subsequently, the toluene-polluted 20% O_2/N_2 stream was passed through the sample for adsorption saturation. Finally, by turning on EMIH (setting 24.3 mT of altering magnetic field, Table S1), toluene was oxidized over the monolithic catalyst in the pollutant atmosphere for 20 min. The variation of chemical bonds during adsorption and oxidation was detected by FTIR spectroscopy. *In situ* FTIR spectroscopy was also conducted in a pure N_2 atmosphere to inspect the oxidation of toluene by lattice oxygen on the monolithic catalyst.

2.4. Activity Test. A monolithic catalyst (4 × 3 cm) was rolled-up and loaded in a quartz tube (φ = 6 mm). The performance in catalyzing thermal oxidation of toluene was evaluated by a fixed bed equipped with resistance furnace (Figure S3). The magnetocaloric oxidation of toluene was conducted on a fixed bed configured with an EMIH device, as shown in Figure S2. The EMIH device was operated at handling conditions of 24.2 V and 2.8 A, which could generate 24.3 mT of alternating magnetic field in the reaction area (Table S1). A 20% O_2/N_2 stream containing 1000 ppm toluene was passed through the bed layer with a rate of 66 mL/min, resulting in a gas hourly space velocity (GHSV) of 4668 h^{-1}. The catalytic performance was evaluated by toluene conversion and mineralization. The calculation equations are as follows.

$$\text{toluene conversion (\%)} = ([\text{toluene}]_{in} - [\text{toluene}]_{out})/[\text{toluene}]_{in} \times 100\% \quad (1)$$

https://doi.org/10.1021/acs.est.3c09541
Environ. Sci. Technol. XXXX, XXX, XXX−XXX

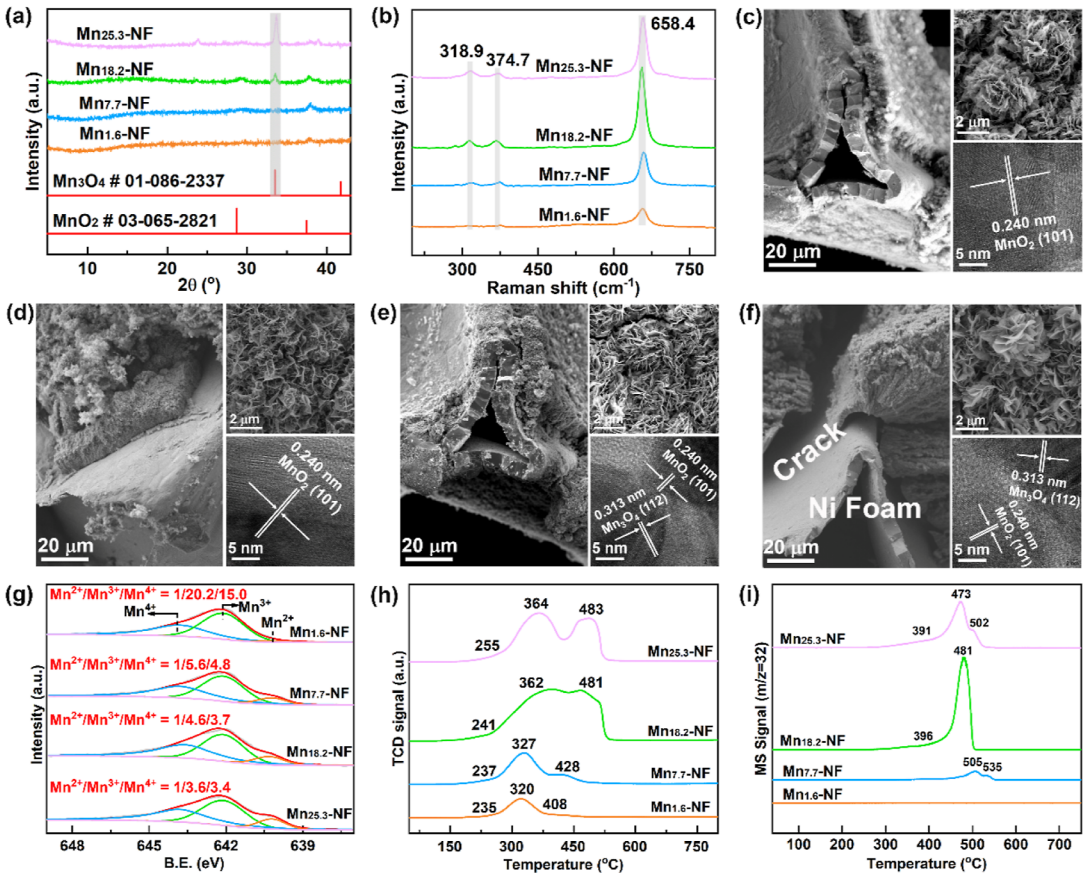

Figure 1. Structural and physicochemical characterization of all the samples. (a) XRD patterns of Mn_x-NF in the range of 5−43°. (b) Raman spectra of Mn_x-NF. (c−f) SEM cross-sectional images, SEM surface images, and TEM images of $Mn_{1.6}$-NF, $Mn_{7.7}$-NF, $Mn_{18.2}$-NF, $Mn_{25.3}$-NF, respectively. (g) Mn 2p spectra of Mn_x-NF. (h) H_2-TPR profiles measured by the TCD. (i) O_2-TPD results measured by online MS.

$$\text{mineralization}\ (\%) = [CO_2]_{out}/[CO_2]_{complete} \times 100\% \quad (2)$$

$[\text{toluene}]_{in}$, $[\text{toluene}]_{out}$, $[CO_2]_{out}$, and $[CO_2]_{complete}$ correspond to the initial toluene concentration, outlet toluene concentration, outlet CO_2 concentration, and CO_2 concentration when toluene was completely oxidized, respectively.

3. RESULTS AND DISCUSSION

3.1. Textural and Physicochemical Characterization.

The Mn_x-NF monolithic catalysts were prepared by electrodepositing MnO_x on a nickel foam (NF) support (as illustrated by Figure S4). Actual Mn contents of $Mn_{1.6}$-NF, $Mn_{7.7}$-NF, $Mn_{18.2}$-NF, and $Mn_{25.3}$-NF monolithic catalysts were 1.6, 7.7, 18.2, and 25.3 wt %, respectively, which were determined by XRF (Figure S1). The XRD patterns (Figure S5) of Mn_x-NF monolithic catalysts show obvious characteristic peaks of Ni species, and the signal peaks gradually become weaker as the load mass increases, suggesting that the MnO_x coating covers the NF successfully. Furthermore, the specific XRD patterns of Mn_x-NF in the range of 5−43° (Figure 1a) show that $Mn_{1.6}$-NF and $Mn_{7.7}$-NF monolithic catalysts exhibit the weak diffraction characteristic of the MnO_2 phase (MnO_2 # 03-065-2821) and the apparent Mn_3O_4 phase (Mn_3O_4 #01-086-2337) appears on $Mn_{18.2}$-NF and $Mn_{25.3}$-NF monolithic catalysts. Moreover, in the Raman spectra (Figure 1b), the three peaks at 658.4, 374.7, and 318.9 cm^{-1} are characteristic of the Mn−O vibration modes of Mn_3O_4,[24,25] confirming the formation of Mn_3O_4.

SEM and TEM images were obtained to probe the morphology and microstructure of the Mn_x-NF monolithic catalysts. SEM cross-sectional images of Mn_x-NF (left portion of Figure 1c−f) present the attachment state between MnO_x and NF. As the percentage of Mn reaches 25.3 wt %, cracks appear between MnO_x and the support (Figure 1f). As shown in the top right of Figure 1c−f, all Mn_x-NF samples have a flower-like hierarchical structure composed of MnO_x sheets, which is conducive to increasing the contact between the reaction substrate and Mn_x-NF catalysts. TEM images (bottom right part of Figure 1c,d) of $Mn_{1.6}$-NF and $Mn_{7.7}$-NF disclose that the resolved lattice fringe is 0.240 nm, which can be assigned to the (101) plane of MnO_2. For $Mn_{18.2}$-NF and $Mn_{25.3}$-NF, the lattice spacings of 0.240 and 0.313 nm corresponding to MnO_2 (101) and Mn_3O_4 (112) lattice planes, respectively, can be observed in the bottom right part of Figure 1e,f.[25] The above observation results are in accordance with XRD patterns, proving that crystalline phases of surface components change from MnO_2 to Mn_3O_4 with a prolonged electrodeposition time.

XPS spectra were employed to reveal the oxidation states of metal ions and oxygen species on the surface of the Mn_x-NF monolithic catalysts. As presented in Figure 1g, the Mn 2p XPS profiles of the Mn_x-NF could be divided into three peaks at 643.8, 642.1, and 641.2 eV, corresponding to the Mn^{4+}, Mn^{3+}, and Mn^{2+} species, respectively.[18] As the Mn loading increases, a higher proportion of Mn^{2+} gradually appears on the surface of catalysts, which is reflected in the regular modification of the $Mn^{2+}/Mn^{3+}/Mn^{4+}$ ratio from a 1/20.2/15.0 ratio for $Mn_{1.6}$-NF

https://doi.org/10.1021/acs.est.3c09541
Environ. Sci. Technol. XXXX, XXX, XXX−XXX

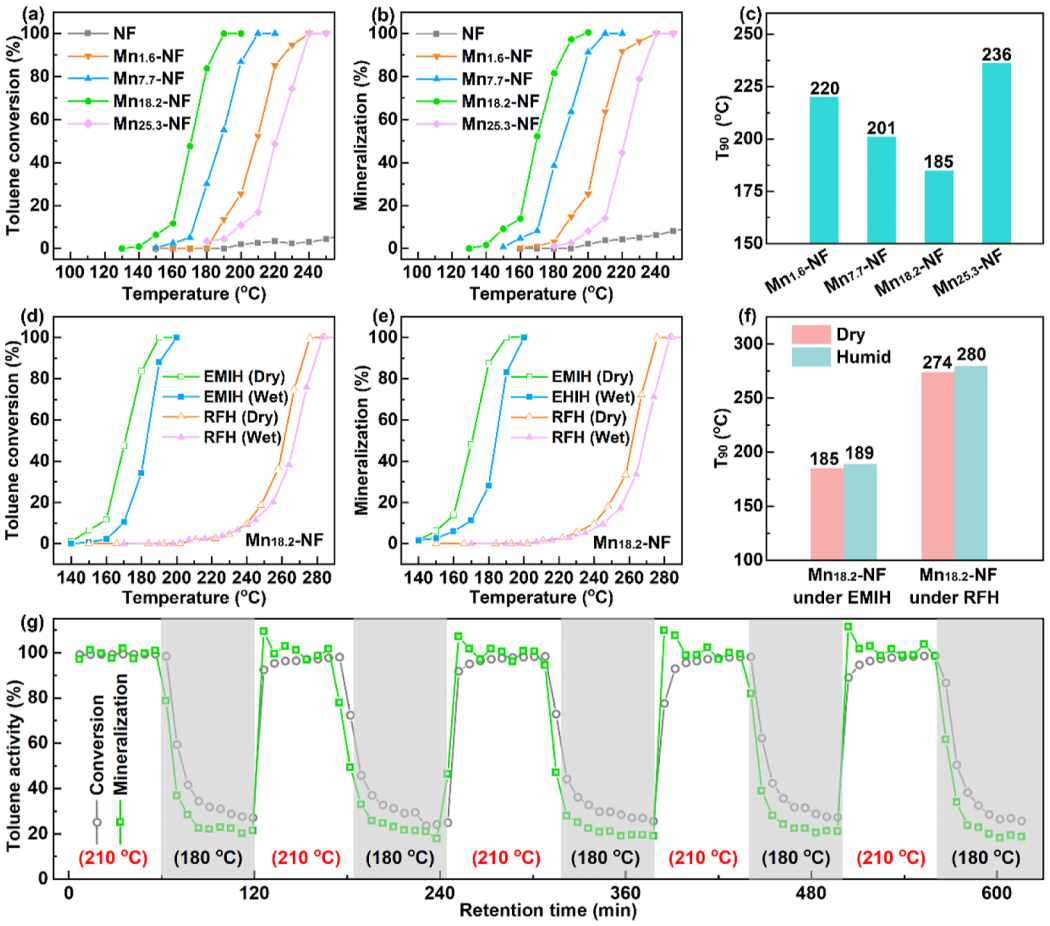

Figure 2. Evaluation of the catalytic performance in removing toluene. (a,b) Activity profiles from perspectives of conversion and mineralization under conditions of 1000 ppm toluene, 20% O_2/N_2, EMIH driven, and GHSV = 4668 h^{-1}. (c) 90% of conversion (T_{90}) of Mn_x-NF monolithic catalysts. (d,e) Activity profiles of the $Mn_{18.2}$-NF catalyst from the perspectives of conversion and mineralization under conditions of 1000 ppm toluene, 5 vol % H_2O (when used), 20% O_2/N_2, EMIH or RFH condition, and WHSV = 44,000 mL/(g h) (based on MnO_x). (f) T_{90} of the $Mn_{18.2}$-NF monolithic catalyst. (g) Catalytic stabilities of $Mn_{18.2}$-NF for different conversion conditions of containing 1000 ppm toluene, 5 vol % H_2O, and WHSV = 44,000 mL/(g h) (based on MnO_x).

to the 1/3.6/3.4 ratio for $Mn_{25.3}$-NF. It is ascribed to the thickness of the MnO_x coating because the thicker MnO_x coating accompanied by the higher overpotential prohibits oxidation of Mn^{2+} ions. The O 1s XPS profile (Figure S6) could be fitted into three peaks belonging to hydroxyl oxygen ($O_{(-OH)}$), adsorbed oxygen (O_{ads}), and lattice oxygen (O_{latt}), respectively.[18] The O_{latt}/O_{ads} ratios decrease with the increasing Mn loading. The similar changing tendencies of $Mn^{2+}/Mn^{3+}/Mn^{4+}$ and O_{latt}/O_{ads} ratios indicate the relationship between the low-valence Mn cations existing and the generation of surface adsorbed oxygen. Meanwhile, binding energies of O_{latt} and O_{ads} species also increase with Mn loading, suggesting the activation of O_{latt} with lower electron cloud density.[26,27]

The influence of Mn loading on the reducibility was examined by H_2-TPR and is displayed in Figure 1h. The reduction of Mn_x-NF occurs in three distinct steps: 235−255 °C (peak α), 320−364 °C (peak β), and 408−483 °C (peak γ). Peak α observed at a low temperature (235−255 °C) is due to the weakly adsorbed oxygen species.[28] Peaks β and γ correspond to the process of $MnO_2 \rightarrow Mn_3O_4 \rightarrow MnO$.[28] As the thickness of the Mn layer increases, the peaks β and γ are shifted to higher temperatures, which can be ascribed to the fact that the low-valence Mn in the surface layer hinders the reduction of high-valence Mn in the inner layer according to the above structural analysis. An O_2-TPD test (Figure 1i) was performed to inspect the mobility of oxygen components. Desorption peaks at 391−396 and 473−535 °C are assigned to surface active oxygen species and lattice oxygen species, respectively.[28] The desorption temperature for lattice oxygen can be ranked in the following order: $Mn_{25.3}$-NF (473 °C) → $Mn_{18.2}$-NF (481 °C) → $Mn_{7.7}$-NF (505 °C). The lower desorption temperature confirms that the activated O_{latt} on the surface promotes oxygen mobility, which corresponds to the XPS analysis of O 1s.

3.2. Performance in Toluene Oxidation. The performance of monolithic catalysts in catalytic oxidation toluene was first evaluated by applying EMIH as the heating source. The activities are assessed on the basis of toluene conversion and CO_2 rising, namely, mineralization (Figure 2a,b). As depicted by Figure 2a, pristine NF has no activity to catalyze toluene oxidation, thereby resulting in rare conversion even if the temperature reaches above 250 °C, which implies the dominant role of MnO_x for catalytic oxidation. The performance is, in fact, influenced by MnO_x loading. The changing tendencies of toluene conversion and mineralization about temperature are similar. The shift of activity curves suggests that the temperature for removal of toluene on $Mn_{18.2}$-NF is

https://doi.org/10.1021/acs.est.3c09541
Environ. Sci. Technol. XXXX, XXX, XXX−XXX

Table 1. Summary of Previous Research Papers on Toluene Oxidation[38−54]

catalyst	catalytic mode	reaction conditions	T_{90} (°C)	ref.
flower-like Mn_2O_3	thermal catalysis	1000 ppm, 20,000 mL/(g h), 20% O_2/N_2, 100 mg of the catalyst	238	38
α-MnO_2-Mn_{4c}	thermal catalysis	1000 ppm, 60,000 mL/(g h), 20% O_2/N_2, total rate 200 mL/min, 200 mg of the sample	222	39
MnO_x	thermal catalysis	500 ppm, 60,000 h^{-1}, 20% O_2/N_2, 0.1 mL of the catalyst	238	40
MnO-250	photothermal catalysis	170 ppm, 45,000 mL/(g h), 20% O_2/N_2, 393 mW/cm^{-2}	212	41
Co_1/MnO_2	thermal catalysis	1000 ppm, 60,000 mL/(g h), 20% O_2/N_2, 66 mg of the catalyst	260	42
CuO-MnO_x	thermal catalysis	1000 ppm, 60,000 mL/(g h), 20% O_2/N_2, 66 mg of the catalyst	225	43
5.0% Ce/OMS	thermal catalysis	1000 ppm, 60,000 mL/(g h), 20% O_2/N_2, 66.6 mg of the catalyst	230	44
9 wt % MnO_x-CeO_2	photothermal catalysis	100 ppm, 60,000 mL/(g h), 20% O_2/N_2	210	45
Pt/α-MnO_2	thermal catalysis	1000 ppm, 60,000 mL/(g h), 20% O_2/N_2	170	46
Ag/δ-MnO_2	thermal catalysis	1000 ppm, 60,000 mL/(g h), 20% O_2/N_2, 100 mg of the catalyst	224	47
Au/3DOM Mn_2O_3	thermal catalysis	1000 ppm, 40,000 mL/(g h), 20% O_2/N_2	244	48
0.65Pt/Mn-TiO_2	photothermal catalysis	200 ppm, 56,250 mL/(g h), 20% O_2/N_2, 20 mg of the catalyst	195	49
Co−Fe monolithic catalyst	thermal catalysis	200 ppm, 10,000 h^{-1}, 20% O_2/N_2, a 1.8 × 1.8 × 0.9 cm cube of the catalyst	347	50
Pt/TiO_2 monolithic catalysts	thermal catalysis	2000 ppm, GHSV = 3000 h−^{1}, WHSV = 370,000 mL/(g h) (based on Pt/TiO_2), 20% O_2/N_2	212	51
Pt/CuMnCe monolithic catalyst	thermal catalysis	2000 ppm, 5000 h^{-1}, 20% O_2/N_2, 10 mm diameter and 50 mm length of the cylindrical cordierite honeycomb	216	52
Co_2AlO_4/Ni foam monolithic catalyst	thermal catalysis	1000 ppm, 10,000 h^{-1}, 20% O_2/N_2, 5 cm × 7 cm × 1.6 mm of Ni foam	272	53
MnO_2-O_v/CF monolithic catalyst	thermal catalysis	1000 ppm, 10,000 h^{-1}, 20% O_2/N_2, a 1.5 cm × 1.0 cm Ni piece	215	54
$Mn_{18.2}$-NF monolithic catalyst	thermal catalysis	1000 ppm, GHSV = 4668 h−^{1}, WHSV = 44,000 mL/(g h) (based on MnO_x), 20% O_2/N_2, 3 cm × 4 cm × 1.6 mm of Ni foam, RFH	274	this work
$Mn_{18.2}$-NF monolithic catalyst	electromagnetic thermal catalysis	1000 ppm, GHSV = 4668 h−^{1}, WHSV = 44,000 mL/(g h) (based on MnO_x), 20% O_2/N_2, 3 cm × 4 cm × 1.6 mm of Ni foam, EMIH	185	this work

remarkably lower than those of the others. Considering the temperature for 90% conversion (T_{90}) as an assessment rule, an inverted volcanic tendency is presented in Figure 2c. The decrease of T_{90} with MnO_x loading is due to the increased content of the active site, but $Mn_{25.3}$-NF with higher MnO_x loading requires higher T_{90} than $Mn_{18.2}$-NF. According to the discussion about H_2-TPR and O_2-TPD, $Mn_{25.3}$-NF exhibits comparable reducibility and oxygen reactivity to $Mn_{18.2}$-NF, which is commonly thought to perform a similar activity. In our opinion, this opposite result is related to the separation between the MnO_x coating and Ni foam, causing more difficulty in delivering energy from the magnetocaloric support to the active site under the EMIH condition. In the control experiment, the interface between the manganese oxide layer and Ni foam of $Mn_{18.2}$-NF could be destroyed through mechanical friction, resulting in $Mn_{18.2}$-NF-S with a looser interface, as shown by Figure S7. The activity of $Mn_{18.2}$-NF-S is significantly reduced compared to that of $Mn_{18.2}$-NF under EMIH, so its ignition curve is shifted to a higher temperature of about 30 °C, as depicted by Figure S8, which implies the important role of the metal oxide−support interaction in EMIH-driven catalytic oxidation.

$Mn_{18.2}$-NF is screened out to investigate the influence of different heating models involving EMIH and RFH on the catalytic performance. At ideal conditions without humidity, T_{90} for EMIH-driven catalytic oxidation of toluene is about 89 °C, lower than that for RFH-driven catalytic oxidation (Figure 2d,f). Although the introduction of 5 vol % H_2O has a slight negative effect on eliminating toluene, the demanded temperatures for EMIH-driven catalysis are still much lower than those for traditional oxidation depending on RFH (Figure 2d,e). In practice, apart from the influence of water vapor, the stability under various temperature switchings should be considered. The robust property of the EMIH-driven system for removal of toluene on $Mn_{18.2}$-NF is examined by repeatedly modifying temperature. As shown in Figure 2g, 1000 ppm toluene is completely oxidized into CO_2 at 210 °C; when temperature decreases to 180 °C toluene conversion and mineralization are about 25% and decline gradually due to accumulation of intermediates, and then, upon elevating the temperature to 210 °C, conversion returns to 100%, and mineralization increases to even higher than 100% at the initial stage owing to the deep oxidation of these intermediates. The cycling test is repeated steadily for 5 times during 10 h. To further clarify the difference between EMIH and RFH, toluene oxidation experiments in a N_2 atmosphere were performed under EMIH and RFH conditions. As seen in Figure S9a,b, a small amount of toluene is converted in both EMIH and RFH conditions, indicating that lattice oxygen is involved in the reaction. But toluene conversion eventually tends to 0 without the supplement of O_2, manifesting that $Mn_{18.2}$-NF would activate the O_2 molecules to supply the reaction, which follows the classic Mars−van Krevelen mechanism. Moreover, the lower temperature of toluene conversion shows that EMIH is beneficial to the activation of oxidizing species compared to RFH.

In order to understand its technologic merits, the EMIH-driven system is compared with other recent studies from four aspects, namely, the metal material, architecture, energy inputting method, and reaction temperature. As listed in Table 1, Mn-containing catalysts usually outperform other tradition metal oxides and exhibit activity comparable to that of supported precious metals in catalytic oxidation of toluene. The values of T_{90} demanded by Mn-containing catalysts mostly fall in between 210 and 250 °C when thermal catalytic oxidation of toluene is powered by resistance furnace or light illumination. Monolithic catalysts prepared through coating active species on a ceramics honeycomb or metallic foam are

https://doi.org/10.1021/acs.est.3c09541
Environ. Sci. Technol. XXXX, XXX, XXX−XXX

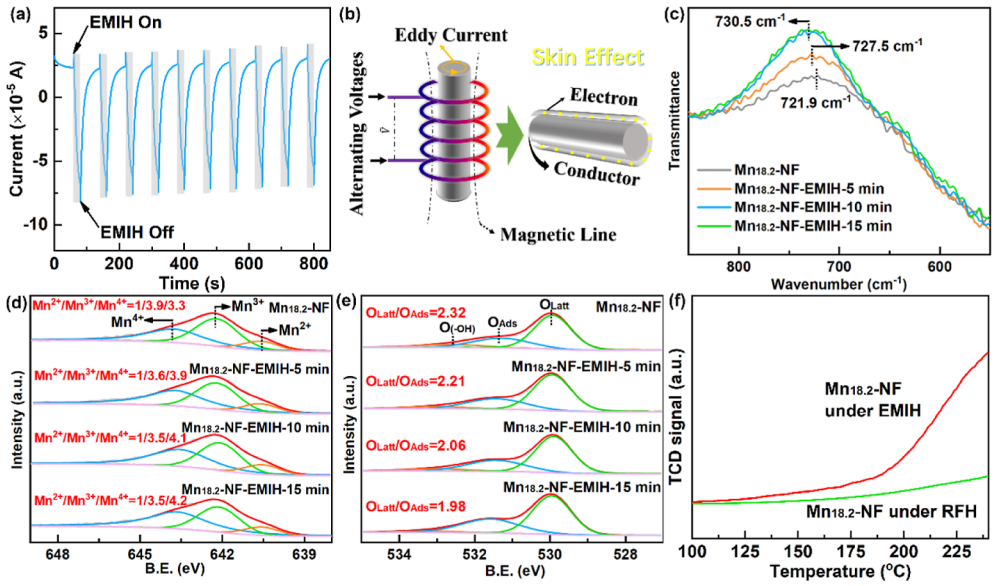

Figure 3. Inspecting the influence of EMIH on structural properties. (a) $i-t$ curve of $Mn_{18.2}$-NF obtained at power on/off EMIH. (b) Schematic elucidation of the influence of EMIH. (c) FTIR spectra of $Mn_{18.2}$-NF, $Mn_{18.2}$-NF-5 min, $Mn_{18.2}$-NF-10 min, and $Mn_{18.2}$-NF-EMIH-15 min. (d) Mn 2p XPS spectra of $Mn_{18.2}$-NF, $Mn_{18.2}$-NF-EMIH-5 min, $Mn_{18.2}$-NF-EMIH-10 min, and $Mn_{18.2}$-NF-EMIH-15 min. (e) O 1s XPS spectra of $Mn_{18.2}$-NF, $Mn_{18.2}$-NF-EMIH-5 min, $Mn_{18.2}$-NF-EMIH-10 min, and $Mn_{18.2}$-NF-EMIH-15 min. (f) H_2-TPR conducted at conditions of EMIH and RFH.

preferred by practical applications owing to the lower pressure drop and easy installation. However, the reaction temperature of monolithic catalysts is usually higher than that of powder catalysts. This is because monolithic catalysts expose fewer active sites than powdered catalysts under the same volume conditions and monolithic catalysts have limited gas−solid transfer compared to powders. Among non-noble monolithic catalysts, the T_{90} of $Mn_{18.2}$-NF under EMIH is 185 °C, which is the lowest. Ni foam of $Mn_{18.2}$-NF not only serves as monolithic support but also as a translator that receives, converts, and delivers electromagnetic energy to the MnO_x coating directly. As shown in Figure S10, the MnO_x layer on Ni foam could be heated to as high as 305 °C by EMIH at 23.8 mT. However, individual MnO_x powders could be self-heated to only 60 °C by EMIH with the same intensity, which is insufficient to trigger toluene oxidation.

3.3. Promotive Effect of the Skin Effect Induced by EMIH. To further understand the promotion effect of EMIH, induced voltage and induced current under EMIH were detected by an electrochemical workstation. As shown in Figure S11, the alternating magnetic field causes an induced electromotive force in the opposite direction of the original potential. As a result, the induced current (Figure 3a) also exhibits the same orientation as the induced voltage due to the same direction of the induced electromotive force and the induced current. After turning off the EMIH device, the current value gradually returns to the initial level. Moreover, in the control experiment (Figure S12), $Mn_{18.2}$-NF (ΔI = 3.8 × 10−4) shows a stronger current response than Ni foam (ΔI = 4.5 × 10^{-6}), indicating the association between the MnO_x layer and Ni foam. The above results prove that eddy current is generated inside the monolithic catalyst under EMIH conditions (illustration in the left part of Figure 3b). And meanwhile, the high-frequency current forces alternating current to the surface of the monolithic catalyst in the form of a thin layer,[29] which causes the skin effect (illustration in the right part of Figure 3b).

In order to investigate the influence of the skin effect on the chemical bonds of MnO_x, FTIR spectra of $Mn_{18.2}$-NF, $Mn_{18.2}$-NF-EMIH-5 min, $Mn_{18.2}$-NF-EMIH-10 min, and $Mn_{18.2}$-NF-EMIH-15 min were analyzed (Figure 3c). The absorption band at 721.9 cm^{-1} is assigned to the vibration absorption superposition of the Mn−O−Mn bridging oxygen bond.[18] After treatment by EMIH for 5 min in an air atmosphere, the infrared absorption band of the Mn−O−Mn structure shifts from 721.9 to 727.5 cm^{-1} and further shifts to 730.5 cm^{-1} when treatment time reaches over 10 min, indicating that the bond energy is strengthened due to modification on the microstructure. In addition, the surface chemical states were further investigated by XPS patterns. The Mn 2p spectra shown in Figure 3d can be deconvoluted into three peaks at 643.8 eV, 642.3, and 641.0 eV, corresponding to Mn^{4+}, Mn^{3+}, and Mn^{2+} species, respectively.[18] Based on the peak integration, the ratio values of $Mn^{2+}/Mn^{3+}/Mn^{4+}$ are 1/3.9/3.3 for $Mn_{18.2}$-NF, 1/3.6/3.9 for $Mn_{18.2}$-NF-EMIH-5 min, 1/3.5/4.1 for $Mn_{18.2}$-NF-EMIH-10 min, and 1/3.5/4.2 for $Mn_{18.2}$-NF-EMIH-15 min. It indicates that the content of Mn^{4+} increases with EMIH, but a promotion ceiling appears with prolonged treatment, which is in accordance with the previous discussion about FTIR spectroscopy. It should be noted that there is no obvious change arising to the matrix lattice of the MnO_x layer on $Mn_{18.2}$-NF with EMIH-induced growth of the Mn valence, as evidenced by the XRD patterns in Figure S13. In general, it is accepted that the larger proportion of high-valence Mn corresponds to the tinier quantity of oxygen vacancies.[30] Therefore, the increase of the manganese valence state manifests that the skin effect promotes the electron donating ability of low-valence manganese and reduces defect sites. Active electron donors require suitable electron acceptors. The oxygen molecule is the most direct electron acceptor in this reaction system. Thus, the XPS spectra of O 1s analysis are given in Figure 3e. The values of O_{latt}/O_{ads} are 2.32, 2.21, 2.06, and 1.98 for $Mn_{18.2}$-NF, $Mn_{18.2}$-NF-EMIH-5 min, $Mn_{18.2}$-NF-EMIH-10 min, and $Mn_{18.2}$-NF-EMIH-15 min, respectively, indicating that more

https://doi.org/10.1021/acs.est.3c09541
Environ. Sci. Technol. XXXX, XXX, XXX−XXX

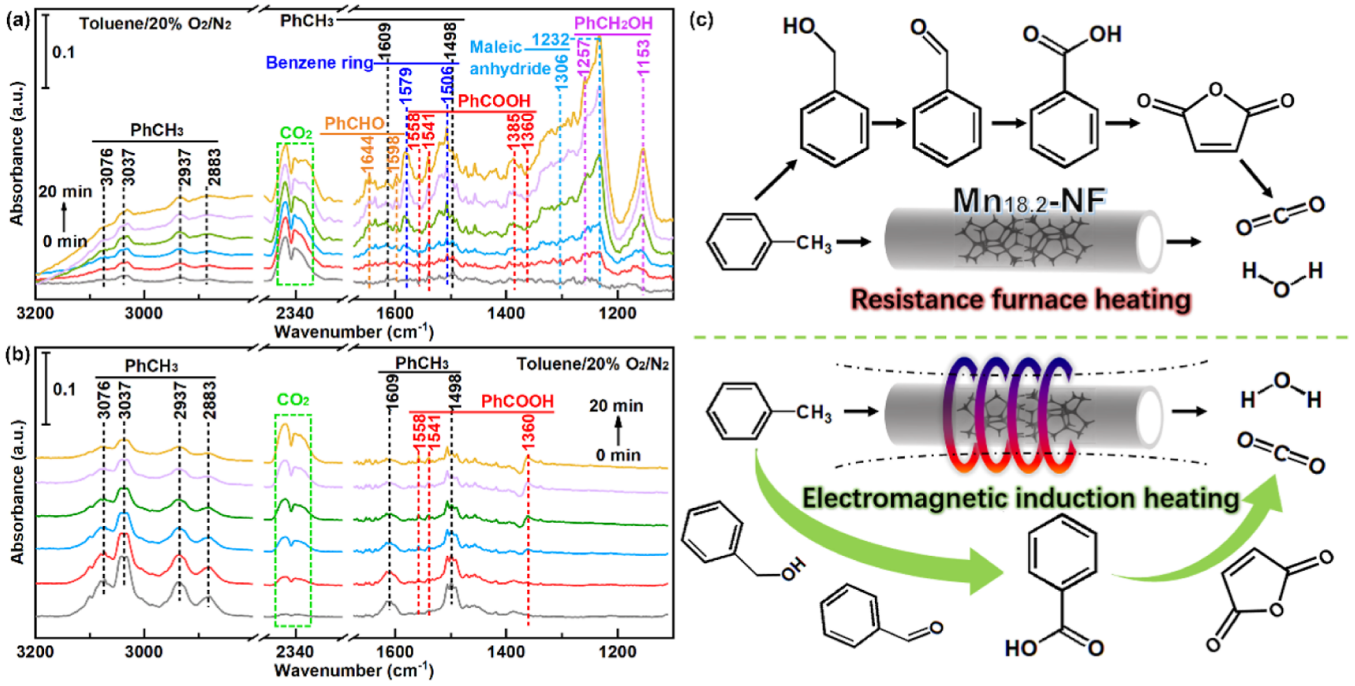

Figure 4. Exploitation of the mechanism of toluene catalytic oxidation driven by different heating models. (a) *In situ* DRIFTS results of RFH-driven catalytic oxidation of toluene in a 20% O_2/N_2 atmosphere on $Mn_{18.2}$-NF at 200 °C. (b) *In situ* FTIR results of catalytic oxidation of toluene in a 20% O_2/N_2 atmosphere on $Mn_{18.2}$-NF that was heated to about 200 °C by EMIH of 24.3 mT intensity. (c) Illustration of the proposed mechanism of catalytic oxidation of toluene driven by different heating models.

surface adsorbed oxygen species (such as O_2^-, and O^-) occupy the above reduced defect sites due to facilitation of the skin effect. O_{ads} tends to participate into the oxidation reaction due to its high activity and the interaction with reactants,[30,31] which also explains why the activity under EMIH is better than the activity of the same sample under RFH.

According to the above discussion, the aggregation of surface electrons in a high-frequency electromagnetic field promotes electron donation from low-valence Mn to molecular oxygen, resulting in an increase of the high-valence Mn cation and surficial adsorbed oxygen species, which has an inevitable effect on reducibility. To investigate the influence, H_2-TPR was conducted by using EMIH at the same conditions as those of traditional RFH-driven H_2-TPR. As presented in Figure 3f, EMIH-driven reduction of $Mn_{18.2}$-NF is obviously faster than that heated by RFH with the same heating rate of 10 °C/min, implying the stronger enhancement of oxygen reactivity by EMIH than by RFH. To further explore the role of the skin effect in the reaction process, a Toluene-TPSR experiment was conducted in 20% O_2/N_2 or N_2 atmospheres under EMIH or RFH conditions. As shown in Figure S14, under the same heating mode, the output of CO_2 over the $Mn_{18.2}$-NF monolithic catalyst in a 20% O_2/N_2 atmosphere is higher than that in a N_2 atmosphere, indicating that gaseous oxygen is involved in the reaction. Compared with the temperature of the CO_2 curve under the RFH-driven condition in an air atmosphere (bule line), the CO_2 curve under the EMIH condition (red line) obviously shifts to lower temperature, which means that the EMIH mode is conducive to the activation of gaseous oxygen at low temperature. Therefore, EMIH boosts catalytic oxidation of toluene at relatively lower temperature.

3.4. Investigation of the Reaction Mechanism under EMIH. For the purpose of gaining more foundational perceptions into the catalytic toluene oxidation mechanism under RFH and EMIH, *in situ* DRIFTS and *in situ* FTIR spectroscopy were applied for tracking the variation of intermediate species. Figure 4a exhibits a series of *in situ* DRIFTS spectra over the $Mn_{18.2}$-NF catalyst under RFH at a toluene atmosphere. When a toluene-polluted 20% O_2/N_2 stream is introduced into the reaction cell at room temperature, characteristic peaks of toluene could be observed at 3076, 3037, 2937, 2883, 1609, and 1498 cm^{-1} (Figure S15), which confirms that toluene adsorbed on the surface of the $Mn_{18.2}$-NF catalyst.[32,33] As the temperature is increased to 200 °C by RFH, intermediate products such as benzyl alcohol, benzaldehyde, benzoate, and maleic anhydride gradually accumulate and the CO_2 intensity increases slightly, indicating the accumulation of intermediates on the catalyst. As a contrast, Figure 4b shows the dynamic changes in the FTIR spectra of $Mn_{18.2}$-NF under EMIH at a toluene atmosphere. The *in situ* reaction cell under EMIH adopts the infrared transmission technique, therefore showing a more obvious infrared absorption signal (Figure S16). After the EMIH is turned on, the characteristic bands of toluene are in decline, and the CO_2 peak increases significantly. It is worth noting that only the accumulation of benzoic acid species is observed. This is because the ring-opening process is the rate-determining step in the catalytic oxidation of toluene, which easily leads to the accumulation of benzoic acid.[34] The above results indicate that EMIH is conducive to the rapid conversion of intermediates. Similar *in situ* IR results obtained in a N_2 atmosphere (Figures S17 and S18) indicate that lattice oxygen is activated to participate in the oxidation reaction, which is believed to be in accordance with the Mars–van Krevelen mechanism. Combining with activity data in Section 3.2 and characterization analysis in Section 3.3, we can draw a conclusion that the skin effect induced by EMIH is beneficial

https://doi.org/10.1021/acs.est.3c09541
Environ. Sci. Technol. XXXX, XXX, XXX−XXX

fro activating the O_2 molecules and surface oxygen species, which directly promotes the conversion of intermediates.

To further determine the reaction pathway of toluene oxidation, the Toluene-TPO experiment driven by RFH was performed in a N_2 atmosphere. As shown in Figure S19a, the signal intensities of benzyl alcohol, benzaldehyde, and benzoic acid decrease successively, implying that toluene is first oxidized to benzyl alcohol by lattice oxygen, followed by benzaldehyde and benzoic acid. The mass spectrum also detects a weak signal fluctuation of maleic anhydride. And as the temperature increases, the signal of CO_2 reaches the maximum at around 280 °C (Figure S19b). According to other studies on the toluene oxidation mechanism, we can know that toluene oxidation is a stepwise process.[35,36] Therefore, the reaction mechanism of toluene oxidation over $Mn_{18.2}$-NFcan be inferred, as displayed in Figure 4c. Under the condition of RFH, the process of toluene → benzyl alcohol → benzaldehyde → benzoic acid→ maleic anhydride → oxygenated species → CO_2, H_2O is the main reaction pathway for toluene oxidation.[32,37] Differently, a magnetic thermal effect accompanied by the skin effect could promote the enhancement of surface reactive oxygen, resulting in rapid conversion of intermediates, which is favorable to the mineralization of toluene.

3.5. Environmental Significance and Implications. In this study, a monolithic catalyst of Ni foam-supported MnO_x coupled with EMIH is proposed for VOCs degradation, and the mechanism of electromagnetic induction promotion is further revealed. Mn_x-NF catalysts are prepared by the anodic oxidation method, and the $Mn_{18.2}$-NF catalyst is screened out as the optimal catalyst, which displays an excellent catalytic performance for toluene oxidation (T_{90} = 185, 89 °C lower than that for the same catalyst under RFH). Further structural characteristics and *in situ* FTIR spectroscopy prove that the skin effect induced by EMIH facilitates the activation of oxidizing species on the surface and enhances the redox property of the $Mn_{18.2}$-NF monolithic catalyst. The superior reactivity of oxidative species further accelerates the conversion of intermediates, resulting in better performance for eliminating toluene at lower temperature.

In the aspect of theory, this work proposes the facilitating effect of the skin effect induced by EMIH in the catalytic oxidation system, which provides a reference for the development of the electromagnetic induction technology in the environmental field. EMIH has advantages of high efficiency, energy saving, environmental protection, and sustainability, which has been involved in many areas, including magnetic hyperthermia, organic synthesis, catalysis, and so on. This efficient form of energy transmission has a good application prospect in the VOCs control system. Therefore, it is of great significance for air pollution control to further explore the mechanism of activity promotion under electromagnetic conditions to construct a catalytic reaction system driven by electromagnetic induction.

In practical applications, many point source pollutants from VOCs emissions are intermittent and uncertain, which requires an efficient and energy-saving catalytic reaction system. Foam-based monolithic catalysts proposed in this study have good metal plasticity and can be designed into a variety of configurations in different scenarios. The porous structure can also meet the requirements of a low pressure drop and a high surface-to-volume ratio in practical application. Combined with electromagnetic induction, the rapid heating characteristic can achieve flexible applications. We believe that this reaction system can effectively control the widely distributed point source pollution of VOCs. The understanding of the skin effect will provide the basis for the application of electromagnetic induction in the field of environmental catalysis.

■ ASSOCIATED CONTENT

Supporting Information

The Supporting Information is available free of charge at https://pubs.acs.org/doi/10.1021/acs.est.3c09541.

Additional information about detail procedures for catalyst characterization, temperature-programed characterizations (H_2-TPR and O_2-TPD), *in situ* DRIFTS, tables about output magnetic field and assignment of IR bands, photo of the electromagnetic heating device, induced voltage signal, and IR spectra of toluene adsorption (PDF)

■ AUTHOR INFORMATION

Corresponding Authors

Jin Chen − *Xiamen Key Laboratory of Materials for Gaseous Pollutant Control, Institute of Urban Environment, Chinese Academy of Sciences, Xiamen 361021, China; Key Laboratory of Urban Pollutant Conversion, Institute of Urban Environment and CAS Center for Excellence in Regional Atmospheric Environment, Institute of Urban Environment, Chinese Academy of Sciences, Xiamen 361021, China; University of Chinese Academy of Sciences, Beijing 100049, China; College of Resources and Environment, Fujian Agriculture and Forestry University, Fuzhou 350002, China*; Email: jchen@iue.ac.cn

Hongpeng Jia − *Xiamen Key Laboratory of Materials for Gaseous Pollutant Control, Institute of Urban Environment, Chinese Academy of Sciences, Xiamen 361021, China; Key Laboratory of Urban Pollutant Conversion, Institute of Urban Environment and CAS Center for Excellence in Regional Atmospheric Environment, Institute of Urban Environment, Chinese Academy of Sciences, Xiamen 361021, China; University of Chinese Academy of Sciences, Beijing 100049, China;* orcid.org/0000-0001-9558-5563; Email: hpjia@iue.ac.cn

Authors

Chunqi Wang − *Xiamen Key Laboratory of Materials for Gaseous Pollutant Control, Institute of Urban Environment, Chinese Academy of Sciences, Xiamen 361021, China; Key Laboratory of Urban Pollutant Conversion, Institute of Urban Environment and CAS Center for Excellence in Regional Atmospheric Environment, Institute of Urban Environment, Chinese Academy of Sciences, Xiamen 361021, China; University of Chinese Academy of Sciences, Beijing 100049, China; College of Resources and Environment, Fujian Agriculture and Forestry University, Fuzhou 350002, China*

Shuangyong Su − *Xiamen Key Laboratory of Materials for Gaseous Pollutant Control, Institute of Urban Environment, Chinese Academy of Sciences, Xiamen 361021, China; Key Laboratory of Urban Pollutant Conversion, Institute of Urban Environment and CAS Center for Excellence in Regional Atmospheric Environment, Institute of Urban Environment, Chinese Academy of Sciences, Xiamen 361021,*

https://doi.org/10.1021/acs.est.3c09541
Environ. Sci. Technol. XXXX, XXX, XXX−XXX

China; University of Chinese Academy of Sciences, Beijing 100049, China; College of Resources and Environment, Fujian Agriculture and Forestry University, Fuzhou 350002, China

Qiang Li − *Xiamen Key Laboratory of Materials for Gaseous Pollutant Control, Institute of Urban Environment, Chinese Academy of Sciences, Xiamen 361021, China; Key Laboratory of Urban Pollutant Conversion, Institute of Urban Environment and CAS Center for Excellence in Regional Atmospheric Environment, Institute of Urban Environment, Chinese Academy of Sciences, Xiamen 361021, China; University of Chinese Academy of Sciences, Beijing 100049, China*

Xuelong Lv − *Xiamen Key Laboratory of Materials for Gaseous Pollutant Control, Institute of Urban Environment, Chinese Academy of Sciences, Xiamen 361021, China; Key Laboratory of Urban Pollutant Conversion, Institute of Urban Environment and CAS Center for Excellence in Regional Atmospheric Environment, Institute of Urban Environment, Chinese Academy of Sciences, Xiamen 361021, China; University of Chinese Academy of Sciences, Beijing 100049, China*

Zhen Xu − *Xiamen Key Laboratory of Materials for Gaseous Pollutant Control, Institute of Urban Environment, Chinese Academy of Sciences, Xiamen 361021, China; Key Laboratory of Urban Pollutant Conversion, Institute of Urban Environment and CAS Center for Excellence in Regional Atmospheric Environment, Institute of Urban Environment, Chinese Academy of Sciences, Xiamen 361021, China; University of Chinese Academy of Sciences, Beijing 100049, China*

Complete contact information is available at: https://pubs.acs.org/10.1021/acs.est.3c09541

Author Contributions

C.W. conceived the project, performed the experiments, analyzed the data, and wrote the paper. Q.L., X.L., and S.S. took a part in revising the article. Z.X. conducted the XPS test. J.C. participated in writing and revised the article. H.J. supervised the project and revised the manuscript. All the authors contributed to the development of this article. All authors have approved the final version of the article.

Notes

The authors declare no competing financial interest.

■ ACKNOWLEDGMENTS

This work was funded by the STS Program of Fujian Province and CAS [2023T3070]; the National Nature Science Foundation of China [no. 22176187 and 22376193]; the Youth Innovation Promotion Association of CAS [no. 2021304]; and the National Key Research and Development Program of China [no. 2022YFB3504203].

■ REFERENCES

(1) Lu, Y.; Deng, H.; Pan, T.; Liao, X.; Zhang, C.; He, H. Effective toluene ozonation over δ-MnO_2: Oxygen vacancy-induced reactive oxygen species. *Environ. Sci. Technol.* **2023**, *57*, 2918−2927.

(2) Bi, F.; Zhao, Z.; Yang, Y.; Gao, W.; Liu, N.; Huang, Y.; Zhang, X. Chlorine-coordinated Pd single atom enhanced the chlorine resistance for volatile organic compound degradation: Mechanism study. *Environ. Sci. Technol.* **2022**, *56*, 17321−17330.

(3) Yang, Y.; Zhao, S.; Cui, L.; Bi, F.; Zhang, Y.; Liu, N.; Wang, Y.; Liu, F.; He, C.; Zhang, X. Recent advancement and future challenges of photothermal catalysis for VOCs elimination: From catalyst design to applications. *Green Energy Environ.* **2023**, *8*, 654−672.

(4) He, C.; Cheng, J.; Zhang, X.; Douthwaite, M.; Pattisson, S.; Hao, Z. P. Recent advances in the catalytic oxidation of volatile organic compounds: A review based on pollutant sorts and sources. *Chem. Rev.* **2019**, *119*, 4471−4568.

(5) He, F.; Weon, S.; Jeon, W.; Chung, M. W.; Choi, W. Self-wetting triphase photocatalysis for effective and selective removal of hydrophilic volatile organic compounds in air. *Nat. Commun.* **2021**, *12*, 6259.

(6) Xiao, M.; Yang, X.; Peng, Y.; Guo, Y.; Wei, Y.; Ge, M.; Yu, X. Confining shell-sandwiched Ag clusters in MnO_2-CeO_2 hollow spheres to boost activity and stability of toluene combustion. *Nano Res.* **2022**, *15*, 7042−7051.

(7) Chen, J.; Chen, X.; Chen, X.; Xu, W.; Xu, Z.; Jia, H.; Chen, J. Homogeneous introduction of CeO_y into MnO_x-based catalyst for oxidation of aromatic VOCs. *Appl. Catal., B* **2018**, *224*, 825−835.

(8) Xu, H.; Yan, N.; Qu, Z.; Liu, W.; Mei, J.; Huang, W.; Zhao, S. Gaseous heterogeneous catalytic reactions over Mn-based oxides for environmental applications: A critical review. *Environ. Sci. Technol.* **2017**, *51*, 8879−8892.

(9) Yang, R.; Fan, Y.; Ye, R.; Tang, Y.; Cao, X.; Yin, Z.; Zeng, Z. MnO_2-based materials for environmental applications. *Adv. Mater.* **2021**, *33*, 2004862.

(10) Kołodziej, A.; Łojewska, J.; Kleszcz, T. Structured catalytic reactor for VOC combustion. *Polish J. Chem. Technol.* **2007**, *9*, 10−14.

(11) Chen, X.; Li, J.; Wang, Y.; Zhou, Y.; Zhu, Q.; Lu, H. Preparation of nickel-foam-supported Pd/NiO monolithic catalyst and construction of novel electric heating reactor for catalytic combustion of VOCs. *Appl. Catal. A-Gen* **2020**, *607*, 117839.

(12) Lopatin, S.; Elyshev, A.; Zagoruiko, A. Catalytic device for environmentally friendly combustion of liquid fuels on the base of structured glass-fiber catalyst. *Catal. Today* **2022**, *383*, 259−265.

(13) Li, Y.; Zhang, C.; Yu, Y.; Zhang, Z. Design and optimization of VOC control process for tail gas in Rectisol unit based on steady state and dynamic simulation. *Process Saf. Environ. Prot.* **2022**, *168*, 820−832.

(14) Banús, E. D.; Sanz, O.; Milt, V. G.; Miró, E. E.; Montes, M. Development of a stacked wire-mesh structure for diesel soot combustion. *Chem. Eng. J.* **2014**, *246*, 353−365.

(15) Sanz, O.; Banús, E. D.; Goya, A.; Larumbe, H.; Delgado, J. J.; Monzón, A.; Montes, M. Stacked wire-mesh monoliths for VOCs combustion: Effect of the mesh-opening in the catalytic performance. *Catal. Today* **2017**, *296*, 76−83.

(16) Chen, J.; Xu, W.; Li, X.; Wang, C.; Hu, Z.; Jia, H. Combining bi-functional Pt/USY and electromagnetic induction for rapid in-situ adsorption-combustion cycling of gaseous organic pollutant. *J. Hazard. Mater.* **2022**, *426*, 128097.

(17) Wang, C.; Chen, J.; Xu, W.; Li, X.; Jia, H. Cooking-like regeneration prolonging the catalytic lifetime for ambient removal of indoor HCHO. *ACS ES&T Engg* **2022**, *2*, 1229−1238.

(18) Wang, C.; Chen, J.; Li, Q.; Su, S.; Jia, H.; He, H. Unveiling the position effect of Ce within layered MnO_2 to prolong the ambient removal of indoor HCHO. *Environ. Sci. Technol.* **2023**, *57*, 4598−4607.

(19) Wang, W.; Duong-Viet, C.; Tuci, G.; Liu, Y.; Rossin, A.; Luconi, L.; Nhut, J.-M.; Nguyen-Dinh, L.; Giambastiani, G.; Pham-Huu, C. Highly nickel-loaded gamma-alumina composites for a radiofrequency-heated, low-temperature CO_2 methanation scheme. *ChemSusChem* **2020**, *13*, 5468−5479.

(20) Wang, W.; Duong-Viet, C.; Xu, Z.; Ba, H.; Tuci, G.; Giambastiani, G.; Liu, Y.; Truong-Huu, T.; Nhut, J.-M.; Pham-Huu, C. CO_2 methanation under dynamic operational mode using nickel nanoparticles decorated carbon felt (Ni/OCF) combined with inductive heating. *Catal. Today* **2020**, *357*, 214−220.

(21) Zha, K.; Sun, W.; Huang, Z.; Xu, H.; Shen, W. Insights into high-performance monolith catalysts of Co_3O_4 nanowires grown on nickel foam with abundant oxygen vacancies for formaldehyde oxidation. *ACS Catal.* **2020**, *10*, 12127−12138.

(22) Zhao, Q.; Zheng, Y.; Song, C.; Liu, Q.; Ji, N.; Ma, D.; Lu, X. Novel monolithic catalysts derived from in-situ decoration of Co_3O_4 and hierarchical Co_3O_4@MnO_x on Ni foam for VOC oxidation. *Appl. Catal., B* **2020**, *265*, 118552.
(23) Xiao, K.; Lin, R.-T.; Wei, J.-X.; Li, N.; Li, H.; Ma, T.; Liu, Z.-Q. Electrochemical disproportionation strategy to in-situ fill cation vacancies with Ru single atoms. *Nano Res.* **2022**, *15*, 4980−4985.
(24) Yang, L.-X.; Zhu, Y.-J.; Tong, H.; Wang, W.-W.; Cheng, G.-F. Low temperature synthesis of Mn_3O_4 polyhedral nanocrystals and magnetic study. *J. Solid State Chem.* **2006**, *179*, 1225−1229.
(25) Liu, Z.; Wang, M.; Liu, S.; Chen, Z.; Yang, L.; Sun, K.; Chen, Y.; Zeng, L.; Wang, W.; Zhao, J.; Sun, G.; Liu, B.; Pan, Y.; Liu, Y.; Liu, C. Design of assembled composite of Mn_3O_4@Graphitic carbon porous nano-dandelions: A catalyst for Low-temperature selective catalytic reduction of NO_x with remarkable SO_2 resistance. *Appl. Catal., B* **2020**, *269*, 118731.
(26) Yang, W.; Wang, Y.; Yang, W.; Liu, H.; Li, Z.; Peng, Y.; Li, J. Surface in situ doping modification over Mn_2O_3 for toluene and propene catalytic oxidation: the effect of isolated $Cu^{\delta+}$ insertion into the mezzanine of surface MnO_2 cladding. *ACS Appl. Mater. Interfaces* **2021**, *13*, 2753−2764.
(27) Wang, J.; Li, J.; Jiang, C.; Zhou, P.; Zhang, P.; Yu, J. The effect of manganese vacancy in birnessite-type MnO_2 on room-temperature oxidation of formaldehyde in air. *Appl. Catal., B* **2017**, *204*, 147−155.
(28) Wang, Y.; Liu, K.; Wu, J.; Hu, Z.; Huang, L.; Zhou, J.; Ishihara, T.; Guo, L. Unveiling the effects of alkali metal ions intercalated in layered MnO_2 for formaldehyde catalytic oxidation. *ACS Catal.* **2020**, *10*, 10021−10031.
(29) Aiello, G.; Alfonzetti, S.; Rizzo, S. A.; Salerno, N. Optimization of the shape of an induction heating device in the presence of skin effect in the coils. *COMPEL—Int. J. Comput. Math. Electr. Electron. Eng.* **2019**, *39*, 525−531.
(30) Rong, S.; Zhang, P.; Liu, F.; Yang, Y. Engineering crystal facet of α-MnO_2 nanowire for highly efficient catalytic oxidation of carcinogenic airborne formaldehyde. *ACS Catal.* **2018**, *8*, 3435−3446.
(31) Setvin, M.; Aschauer, U.; Scheiber, P.; Li, Y.-F.; Hou, W.; Schmid, M.; Selloni, A.; Diebold, U. Reaction of O_2 with subsurface oxygen vacancies on TiO_2 anatase (101). *Science* **2013**, *341*, 988−991.
(32) Li, Y.; Chen, T.; Zhao, S.; Wu, P.; Chong, Y.; Li, A.; Zhao, Y.; Chen, G.; Jin, X.; Qiu, Y.; Ye, D. Engineering cobalt oxide with coexisting cobalt defects and oxygen vacancies for enhanced catalytic oxidation of toluene. *ACS Catal.* **2022**, *12*, 4906−4917.
(33) Liu, Y.; Li, X.; Chen, D.; Li, N.; Xu, Q.; Li, H.; He, J.; Lu, J. Low quantity of Pt loaded onto $CeCoO_x$ nanoboxes: Surface-rich reactive oxygen species for catalytic oxidation of toluene. *J. Hazard. Mater.* **2023**, *442*, 130065.
(34) Shen, Y.; Deng, J.; Impeng, S.; Li, S.; Yan, T.; Zhang, J.; Shi, L.; Zhang, D. Boosting toluene combustion by engineering Co-O strength in cobalt oxide catalysts. *Environ. Sci. Technol.* **2020**, *54*, 10342−10350.
(35) Mi, R.; Li, D.; Hu, Z.; Yang, R. T. Morphology effects of CeO_2 nanomaterials on the catalytic combustion of toluene: A combined kinetics and diffuse reflectance infrared fourier transform spectroscopy study. *ACS Catal.* **2021**, *11*, 7876−7889.
(36) Shen, Y.; Deng, J.; Hu, X.; Chen, X.; Yang, H.; Cheng, D.; Zhang, D. Expediting toluene combustion by harmonizing the Ce-O strength over Co-doped CeZr oxide catalysts. *Environ. Sci. Technol.* **2023**, *57*, 1797−1806.
(37) He, J.; Li, X.; Wang, Y.; Xiao, J.; Liu, Y.; Li, H.; Li, N.; Xu, Q.; He, J.; Chen, D.; Lu, J. Ni-Mn spinel aerogel catalysts with adsorption induced superior activity for low-temperature toluene oxidation. *Chem. Eng. J.* **2023**, *454*, 140039.
(38) Wang, F.; Dai, H. X.; Deng, J.; Bai, G.; Ji, K.; Liu, Y. Manganese oxides with rod-wire-tube-and flower-like morphologies: Highly effective catalysts for the removal of toluene. *Environ. Sci. Technol.* **2012**, *46*, 4034−4041.
(39) Wang, F.; Deng, J.; Impeng, S.; Shen, Y.; Yan, T.; Chen, G.; Shi, L.; Zhang, D. Unraveling the effects of the coordination number of Mn over α-MnO_2 catalysts for toluene oxidation. *Chem. Eng. J.* **2020**, *396*, 125192.
(40) Zhang, X.; Ma, Z. a.; Song, Z.; Zhao, H.; Liu, W.; Zhao, M.; Zhao, J. Role of cryptomelane in surface-adsorbed oxygen and Mn chemical valence in MnO_x during the catalytic oxidation of toluene. *J. Phys. Chem. C* **2019**, *123*, 17255−17264.
(41) Zhang, M.; Li, G.; Li, Q.; Chen, J.; Elimian, E. A.; Jia, H.; He, H. In situ construction of manganese oxide photothermocatalysts for the deep removal of toluene by highly utilizing sunlight energy. *Environ. Sci. Technol.* **2023**, *57*, 4286−4297.
(42) Jiang, M.; Yan, D.; Lv, X.; Gao, Y.; Jia, H. Recognition of water-dissociation effect toward lattice oxygen activation on single-atom Co catalyst in toluene oxidation. *Appl. Catal., B* **2022**, *319*, 121962.
(43) Xiong, S.; Huang, N.; Peng, Y.; Chen, J.; Li, J. Balance of activation and ring-breaking for toluene oxidation over CuO-MnO_x bimetallic oxides. *J. Hazard. Mater.* **2021**, *415*, 125637.
(44) Chen, J.; Chen, X.; Yan, D.; Jiang, M.; Xu, W.; Yu, H.; Jia, H. A facile strategy of enhancing interaction between cerium and manganese oxides for catalytic removal of gaseous organic contaminants. *Appl. Catal., B* **2019**, *250*, 396−407.
(45) Cao, Y.; Zhang, C.; Xu, D.; Ouyang, X.; Wang, Y.; Lv, L.; Zhang, T.; Tang, S.; Tang, W. Low-temperature oxidation of toluene over MnO_x-CeO_2 nanorod composites with high sinter resistance: Dual effect of synergistic interaction on hydrocarbon adsorption and oxygen activation. *Inorg. Chem.* **2022**, *61*, 15273−15286.
(46) Mo, S.; Zhang, Q.; Zhang, M.; Zhang, Q.; Li, J.; Fu, M.; Wu, J.; Chen, P.; Ye, D. Elucidating the special role of strong metal-support interactions in Pt/MnO_2 catalysts for total toluene oxidation. *Nanoscale Horiz.* **2019**, *4*, 1425−1433.
(47) Yang, W.; Zhao, X.; Wang, Y.; Wang, X.; Liu, H.; Yang, W.; Zhou, H.; Wu, Y. A.; Sun, C.; Peng, Y.; Li, J. Atomically dispersed Ag on δ-MnO_2 via cation vacancy trapping for toluene catalytic oxidation. *Catal. Sci. Technol.* **2022**, *12*, 5932−5941.
(48) Xie, S.; Dai, H.; Deng, J.; Yang, H.; Han, W.; Arandiyan, H.; Guo, G. Preparation and high catalytic performance of Au/3DOM Mn_2O_3 for the oxidation of carbon monoxide and toluene. *J. Hazard. Mater.* **2014**, *279*, 392−401.
(49) Li, G.; Zhang, M.; Chen, J.; Li, Q.; Jia, H. Combined effects of Pt nanoparticles and oxygen vacancies to promote photothermal catalytic degradation of toluene. *J. Hazard. Mater.* **2023**, *449*, 131041.
(50) Xue, T.; Li, R.; Gao, Y.; Wang, Q. Iron mesh-supported vertically aligned Co-Fe layered double oxide as a novel monolithic catalyst for catalytic oxidation of toluene. *Chem. Eng. J.* **2020**, *384*, 123284.
(51) Chen, X.; Zhao, Z.; Zhou, Y.; Zhu, Q.; Pan, Z.; Lu, H. A facile route for spraying preparation of Pt/TiO_2 monolithic catalysts toward VOCs combustion. *Appl. Catal. A-Gen* **2018**, *566*, 190−199.
(52) Zhu, A.; Zhou, Y.; Wang, Y.; Zhu, Q.; Liu, H.; Zhang, Z.; Lu, H. Catalytic combustion of VOCs on Pt/CuMnCe and Pt/CeY honeycomb monolithic catalysts. *J. Rare Earths* **2018**, *36*, 1272−1277.
(53) Mo, S.; Zhang, Q.; Ren, Q.; Xiong, J.; Zhang, M.; Feng, Z.; Yan, D.; Fu, M.; Wu, J.; Chen, L.; Ye, D. Leaf-like Co-ZIF-L derivatives embedded on Co_2AlO_4/Ni foam from hydrotalcites as monolithic catalysts for toluene abatement. *J. Hazard. Mater.* **2019**, *364*, 571−580.
(54) Huang, Q.; Zhao, P.; Lv, L.; Zhang, W.; Pan, B. Redox-induced in situ growth of MnO_2 with rich oxygen vacancies over monolithic copper foam for boosting toluene combustion. *Environ. Sci. Technol.* **2023**, *57*, 9096−9104.

https://doi.org/10.1021/acs.est.3c09541
Environ. Sci. Technol. XXXX, XXX, XXX−XXX